Published in final edited form as:

IEEE Robot Autom Lett. 2023 June ; 8(6): 3725–3731. doi:10.1109/lra.2023.3267008.

Simultaneous Shape and Tip Force Sensing for the COAST Guidewire Robot

Nancy J. Deaton[1] **[Graduate Student Member, IEEE]**, **Timothy A. Brumfiel**[1] **[Graduate Student Member, IEEE]**,

Achraj Sarma[2],

Jaydev P. Desai[1] **[Fellow, IEEE]**

[1]Medical Robotics and Automation (RoboMed) Laboratory, Wallace H. Coulter Department of Biomedical Engineering, Georgia Institute of Technology, Atlanta, GA 30332, USA

Abstract

Placement of catheters in minimally invasive cardiovascular procedures is preceded by navigating to the target lesion with a guidewire. Traversing through tortuous vascular pathways can be challenging without precise tip control, potentially resulting in the damage or perforation of blood vessels. To improve guidewire navigation, this paper presents 3D shape reconstruction and tip force sensing for the COaxially Aligned STeerable (COAST) guidewire robot using a triplet of adhered single core fiber Bragg grating sensors routed centrally through the robot's slender structure. Additionally, several shape reconstruction algorithms are compared, and shape measurements are utilized to enable tip force sensing. Demonstration of the capabilities of the robot is shown in free air where the shape of the robot is reconstructed with average errors less than 2 mm at the guidewire tip, and the magnitudes of forces applied to the tip are estimated with an RMSE of 0.027 N or less.

Keywords

Tendon/Wire Mechanism; Compliant Joints and Mechanisms

I. Introduction

CARDIOVASCULAR diseases (CVDs) are a group of conditions that affect the heart or blood vessels including coronary heart disease, peripheral arterial disease, and many more. CVDs are currently the leading cause of death globally [1] with an estimated 17.9 million deaths in 2019 and cases of heart attack and stroke on the rise [1]. Endovascular

njdeaton@gatech.edu .

[2]Achraj Sarma contributed to the work presented in this paper when he was a graduate student in the RoboMed Laboratory at the Georgia Institute of Technology, Atlanta, GA 30332, USA.

The work reported in this paper was partially presented in a video submitted to the 14th Hamlyn Symposium on Medical Robotics Surgical Robot Challenge, as well as other venues - this video can be viewed at: https://youtu.be/n0M6-B-l-fc

This paper was recommended for publication by Editor Clement Gosselin upon evaluation of the Associate Editor and Reviewers' comments.

interventions typically begin with the navigation of a long, thin wire, known as a guidewire, to the target lesion.

Placement of these wires is conducted manually which results in imprecise tip control as well as the potential to perforate vascular walls during navigation. Many mechanisms have been developed to improve guidance and dexterity for minimally invasive surgeries, such as those to treat CVDs, consisting of tendon-driven mechanisms [2], Shape memory alloy actuated devices [3], concentric tube structures [4], [5], and magnetically actuated wires [6]. The desire to develop precise closed-loop control of these mechanisms is often hindered by the challenges associated with the infinite degrees of freedom and limited feedback from within the small slender structures. As a result, current research has investigated the development of real-time shape sensing of small-scale continuum robots. Some works have aimed to develop such capabilities through medical imaging modalities such as fluoroscopy, which are available in the operating room but should be minimized according to safety practices, ultrasound imaging, which does not require radiation but suffers from low image quality, and magnetic resonance imaging (MRI), which may not be available in the operating room [7]. However, a promising approach towards shape sensing is through the use of fiber Bragg grating (FBG) sensors which can be fixed around a central axis and integrated within slender devices to enable shape sensing [8], [9]. FBG sensors are MRI compatible and can increase the shape sampling rate for robot control [9] or reduce the frequency of x-ray images needed. FBG sensing can be fused with other imaging modalities, such as ultrasound imaging, to improve localization [10]. Furthermore, intrinsic shape sensing can be used to inform the image capture or reconstruction plane.

In addition to shape sensing, force sensing is an active area of research for continuum robotic tools. Force sensing can provide feedback about contact between the surgical tool and tissue to prevent tissue damage or perforation, the latter of which can be fatal [11]. Several works have aimed to use knowledge of the configuration of the robot to estimate forces acting on the robot via intrinsic force sensing through the use of kinematic models [12]–[14], mechanics-based models [15]–[17], and data-driven approaches [18]–[20].

This work aims to equip a micro-scale guidewire robot with intrinsic shape sensing which could be used to inform medical imaging for localization, minimize radiation exposure to clinicians, and provide continuous feedback for navigating through tortuous vasculature. Furthermore, this work aims to facilitate intrinsic force sensing to provide feedback when the tip of the guidewire contacts the vascular wall so that tissue damage and perforation can be prevented. To achieve these goals, FBG fibers are used to combine intrinsic shape and force sensing in a single, slender sensor within the COaxially Aligned STeerable (COAST) guidewire robot. The major contributions of this paper are as follows:

- Incorporation and modelling of an FBG triplet within the COAST guidewire robot, enabling 3D shape reconstruction of an actuated sub-millimeter continuum robot.
- Development of a special micromachined tip for the sub-millimeter guidewire robot which utilizes an FBG segment for both lateral and axial force estimation.

The paper is organized as follows: Section II describes the design of the of the COAST guidewire structure, FBG triplet, a presentation of algorithms utilized to reconstruct the shape of the guidewire robot, and the force sensing approach utilized. Section III includes the calibration of the FBG triplet and force sensing tip, a demonstration of simultaneous shape and force sensing, and an analysis of the various shape reconstruction methods for the guidewire robot. The results are discussed in Section IV. Lastly, conclusions and future work are presented in Section V.

II. Materials and Methods

A. COAST Guidewire Robot Design

The COAST guidewire robot presented in this work, adapted from [21] and [22], consists of 3 coaxially aligned tubes, a fiber Bragg grating sensor triplet, and a tendon. Both the outer and middle tubes are micromachined with unidirectional asymmetric notch (UAN) patterns, using a femtosecond laser (Optec Laser S.A., Frameries, Belgium). These notches allow the guidewire to bend in a single plane. The middle tube is placed within the outer tube with the notches 180° out of phase. Since the tubes develop precurvatures due to asymmetric heating during laser micromachining, placing the tubes 180° out of phase reduces the combined precurvature of the robot. The specifications for the COAST guidewire robot are defined in Table I.

The COAST structure presented in this work, shown in Fig. 1(a), can be segmented into three sections: The non-bending segment, the bending segment, and the force sensing tip. The non-bending segment contains all tubes (inner, middle, outer) while the bending segment contains only the outer and middle tubes. The inner tube can be retracted or inserted to increase or decrease the length of the bending segment of the robot, respectively. The joint is actuated by pulling a nitinol tendon attached to the tip of the middle tube. This tendon is routed through the tubes along the side wall.

A triplet of FBG fibers (described in Section II-B) is routed centrally throughout the structure. The triplet is secured to the outer tube at the beginning of the force sensing tip through the use of micromachined securing plates and epoxy (J-B Weld, Sulphur Springs, Texas). A spring was cut from nitinol tubes and used to fill the space between the outer tube and the FBG triplet within the force sensing tip to prevent buckling of the triplet. Low friction sheaths were placed both between the spring and the outer tube and between the spring and the FBG triplet.

The COAST guidewire robot is actuated by a series of lead screws attached to a brushed DC motor which allow for the tendon to be pulled, the inner tube to be retracted, and the outer tube to be extended. This outward extension of the outer tube allows for motion along the tangent of the curved robot which can be utilized for navigation [23] and for probing. The actuation system is contained within a cylindrical casing attached to a spur gear, enabling 3D motion through rotation. Lastly, the system sits on a larger lead screw assembly allowing for translation of the guidewire stage. The assembly is shown in Fig. 1(b). User inputs for each tube position are used as a reference which is then sent to a PD motor position controller with a disturbance observer.

B. FBG Triplet

Fiber Bragg grating sensors are optical fibers that reflect wavelengths of light dependent on changes in strain and temperature. In this work, 3D shape sensing is achieved using a triplet of three 100 μm diameter FBG fibers (Technica Optical Components, Atlanta, United States), which is similar to the FBG triplet studied in our prior work [24]. A 3D printed rig was used to hold the fibers together at 120° spacing while epoxy was applied to adhere the fibers together along the length of the sensor. Each FBG fiber has three gratings of length 5 mm with 4.39 mm non-sensing length between gratings. The central Bragg wavelengths for the three gratings of each fiber were 1535 nm, 1545 nm, and 1555 nm (provided by the manufacturer) which are measured by a signal interrogator (FBGS International NV, Geel, Belgium). These gratings form the sensing segments of the FBG triplet.

C. Shape Sensing

Each FBG measurement can be utilized to determine the overall shape of the triplet assembly, and thus the shape of the COAST guidewire. The change in the wavelength of light reflected by each fiber is given as [25]:

$$\Delta\lambda_B = K_\varepsilon \Delta\varepsilon + K_T \Delta T \tag{1}$$

where $\Delta\lambda_B$, is the change in the Bragg wavelength, $\Delta\varepsilon$ is the change in strain, and ΔT is the temperature change. The strain sensitivity, K_ε, is 1.2 pm/$\mu\varepsilon$, and the temperature sensitivity, K_T, is 13 pm/°C near the Bragg wavelength of 1550 nm [25], [26]. Assuming constant temperature, the strain in each fiber can be related to the orientation of the neutral axis, θ_j (Figs. 2(a) and 2(b)), radius of curvature, r_j (Fig. 2(b)), and axial strain, ε_j, of the triplet as follows:

$$\varepsilon_{j,1} = \frac{d_{j,1} \sin\left(\theta_j - \frac{2\pi}{3}\right)}{r_j} + \varepsilon_j \tag{2}$$

$$\varepsilon_{j,2} = \frac{d_{j,2} \sin\theta_j}{r_j} + \varepsilon_j \tag{3}$$

$$\varepsilon_{j,3} = \frac{d_{j,3} \sin\left(\theta_j + \frac{2\pi}{3}\right)}{r_j} + \varepsilon_j \tag{4}$$

where j denotes the sensing segment ($j \in \{1, 2, 3\}$). The strains $\varepsilon_{j,1}, \varepsilon_{j,2}, \varepsilon_{j,3}$ denote the strains for fiber 1, fiber 2, and fiber 3, respectively at sensing segment j. The maximum distance

between the fiber core and the neutral axis of the sensor is $d_{j,k}$ where $k \in \{1,2,3\}$ denotes the fiber (Fig. 2(a)). By substituting Eqs. (2), (3), and (4) into Eq. (1), ε_j, θ_j, and the curvature, κ_j, can be obtained from the change in Bragg wavelength of each fiber, $\Delta\lambda_{j,1}, \Delta\lambda_{j,2}$, and $\Delta\lambda_{j,3}$, as follows:

$$\varepsilon_j = \frac{d_{j,2}d_{j,3}\Delta\lambda_{j,1} + d_{j,1}d_{j,3}\Delta\lambda_{j,2} + d_{j,1}d_{j,2}\Delta\lambda_{j,3}}{K_\varepsilon(d_{j,2}d_{j,3} + d_{j,1}d_{j,3} + d_{j,1}d_{j,2})} \tag{5}$$

$$\theta_j = \arctan\left(\frac{3((d_{j,1}+d_{j,3})\Delta\lambda_{j,2} - d_{j,3}\Delta\lambda_{j,1} - d_{j,1}\Delta\lambda_{j,3})}{\sqrt{3}((d_{j,3}-d_{j,1})\Delta\lambda_{j,2} + (d_{j,1}+2d_{j,2})\Delta\lambda_{j,3} - (d_{j,3}+2d_{j,2})\Delta\lambda_{j,1})}\right) \tag{6}$$

$$\kappa_j = \frac{2(a_1\Delta\lambda_{j,1}^2 + a_2\Delta\lambda_{j,2}^2 + a_3\Delta\lambda_{j,3}^2 - b_3\Delta\lambda_{j,1}\Delta\lambda_{j,2} - b_2\Delta\lambda_{j,1}\Delta\lambda_{j,3} - b_1\Delta\lambda_{j,2}\Delta\lambda_{j,3})^{\frac{1}{2}}}{K_\varepsilon\sqrt{3}(d_{j,2}d_{j,3} + d_{j,1}d_{j,3} + d_{j,1}d_{j,2})} \tag{7}$$

where $a_k = d_{j,q}^2 + d_{j,q}d_{j,w} + d_{j,w}^2$ and $b_k = 2d_{j,k}^2 + d_{j,k}(d_{j,q} + d_{j,w}) - d_{j,q}d_{j,w}$ given $q = (k+1) \bmod 3$ and $w = (k+2) \bmod 3$

This calculation can be repeated for each of the three sensing segments. For shape reconstruction, κ and θ can be used to calculate the 3D configuration. Change in length due to axial strain in the guidewire is considered negligible. Various methods have been reported in literature to accomplish shape reconstruction from FBG data [27]–[29]. In this paper, the force sensing tip is isolated from the actuation of the guidewire body. Therefore, interpolation is not performed between sensing segments 2 and 3, and linear interpolation is the highest order polynomial which can be fit between measurements at sensing segments 1 and 2. Since the FBG triplet provides measurement data at the discrete sensing segment locations, interpolation must be performed to estimate the shape of the COAST guidewire between sensing segments. Four reconstruction methods were implemented using different interpolation models, variables, and break points to compare the accuracy of each method in approximating the shape of the COAST guidewire robot as it is actuated through different motion sequences.

Method 1:

$$\kappa(s) = \begin{cases} \kappa_1 \text{ if } s \le l_1 + l_2 \\ \kappa_2 \text{ if } l_1 + l_2 < s \le L_{body} \end{cases} \tag{8}$$

$$\theta(s) = \begin{cases} \theta_1 \text{ if } s \leq l_1 + l_2 \\ \theta_2 \text{ if } l_1 + l_2 < s \leq L_{body} \end{cases} \tag{9}$$

Method 2:

$$\kappa(s) = \begin{cases} \kappa_1 & \text{if } s \leq l_1 \\ \frac{\kappa_2 - \kappa_1}{l_2 + l_3}(s - l_1) + \kappa_1 & \text{if } l_1 < s < l_1 + l_2 + l_3 \\ \kappa_2 & \text{if } l_1 + l_2 + l_3 \leq s \leq L_{body} \end{cases} \tag{10}$$

$$\theta(s) = \begin{cases} \theta_1 \text{ if } s \leq l_1 + l_2 \\ \theta_2 \text{ if } l_1 + l_2 < s \leq L_{body} \end{cases} \tag{11}$$

Method 3:

$$\kappa(s) = \begin{cases} \kappa_1 & \text{if } s \leq l_1 \\ \frac{\kappa_2 - \kappa_1}{l_2 + l_3}(s - l_1) + \kappa_1 & \text{if } l_1 < s < l_1 + l_2 + l_3 \\ \kappa_2 & \text{if } l_1 + l_2 + l_3 \leq s \leq L_{body} \end{cases} \tag{12}$$

$$\theta(s) = \begin{cases} \theta_1 & \text{if } s \leq l_1 \\ \frac{\theta_2 - \theta_1}{l_2 + l_3}(s - l_1) + \theta_1 & \text{if } l_1 < s < l_1 + l_2 + l_3 \\ \theta_2 & \text{if } l_1 + l_2 + l_3 \leq s \leq L_{body} \end{cases} \tag{13}$$

Method 4:

$$\Delta\lambda_k(s) = \begin{cases} \Delta\lambda_{1,k} & \text{if } s \leq l_1 \\ \frac{\Delta\lambda_{2,k} - \Delta\lambda_{1,k}}{l_2 + l_3}(s - l_1) + \Delta\lambda_{1,k} & \text{if } l_1 < s < l_1 + l_2 + l_3 \\ \lambda_{2,k} & \text{if } l_1 + l_2 + l_3 \leq s \leq L_{body} \end{cases} \tag{14}$$

$$d_k(s) = \begin{cases} d_{1,k} & \text{if } s \leq l_1 \\ \frac{d_{2,k} - d_{1,k}}{l_2 + l_3}(s - l_1) + d_{1,k} & \text{if } l_1 < s < l_1 + l_2 + l_3 \\ d_{2,k} & \text{if } l_1 + l_2 + l_3 \leq s \leq L_{body} \end{cases} \tag{15}$$

Eqs. (14) and (15) are substituted into Eqs. (6) and (7) to obtain $\kappa(s)$ and $\theta(s)$. The lengths used for reconstruction are illustrated in Fig. 2(c) and provided in Table II. Break points have been made at the midpoint of each sensing segment, the midpoint between sensing segments 1 and 2, and at the ends of each distinct cutting pattern along the outer tube.

For all reconstruction methods, $\kappa(s)$ and $\theta(s)$ along the force sensing tip are calculated as follows:

$$\kappa(s) = \begin{cases} 0 & \text{if } L_{body} < s < L_{body} + l_5 \\ \kappa_3 & \text{if } L_{body} + l_5 \leq s \leq L_{body} + l_5 + l_6 \\ 0 & \text{if } L_{body} + l_5 + l_6 < s \end{cases} \tag{16}$$

$$\theta(s) = \begin{cases} 0 & \text{if } L_{body} < s < L_{body} + l_5 \\ \theta_3 & \text{if } L_{body} + l_5 \leq s \leq L_{body} + l_5 + l_6 \\ 0 & \text{if } L_{body} + l_5 + l_6 < s \end{cases} \tag{17}$$

The equations for $\kappa(s)$ and $\theta(s)$ are discretized to find $\kappa(i)$ and $\theta(i)$ (where $i \in \{1, 2, \ldots, n\}$). The local change in position in each discrete frame can be calculated as follows:

$$\Delta x(i) = \int_0^{\Delta s} -\sin\theta(i)\sin(\kappa(i)u)du = -\frac{1}{\kappa(i)}[1 - cos(\kappa(i)\Delta s)]sin\theta(i) \tag{18}$$

$$\Delta y(i) = \int_0^{\Delta s} \cos\theta(i)\sin(\kappa(i)u)du = \frac{1}{\kappa(i)}[1 - cos(\kappa(i)\Delta s)]cos\theta(i) \tag{19}$$

$$\Delta z(i) = \int_0^{\Delta s} \cos(\kappa(i)u)du = \frac{1}{\kappa(i)}\sin(\kappa(i)\Delta s) \tag{20}$$

where Δs is the arc length traversed in each discrete step. In this work, a constant $\Delta s = 0.2$ mm was used. The rotation matrix for each step can be calculated as follows:

$$R_i^{i-1} = R_z(\theta(i))R_x(-\kappa(i)\Delta s)R_z(-\theta(i)) \tag{21}$$

where $R_z(\theta)$ and $R_x(\theta)$ represent a rotation by θ about the local z-axis and x-axis, respectively. This can be used to calculate the homogeneous transformation matrix along the length of the sensing section of the guidewire as follows:

$$H_i^0 = H_{i-1}^0 H_i^{i-1} \text{ where } H_i^{i-1} = \begin{bmatrix} R_i^{i-1} & \mathbf{p}_i^{i-1} \\ 0_3^T & 1 \end{bmatrix} \text{ and } \mathbf{p}_i^{i-1} = \begin{bmatrix} \Delta x(i) \\ \Delta y(i) \\ \Delta z(i) \end{bmatrix} \tag{22}$$

D. Tip Force Sensing

The isolated FBG fiber triplet at the tip allows for tip force sensing utilizing the reconstructed shape knowledge. The tip is assumed to have constant material properties and behave like a linear spring in both the lateral and axial directions. This would result in any lateral forces or axial forces following the relationships given by:

$$F_l = K_l \kappa \quad \text{and} \quad F_a = K_a \varepsilon \tag{23}$$

where the lateral force, F_l, is linearly related to curvature, κ, through the lateral stiffness term K_l, and the axial force, F_a, is linearly related to strain, ε, through the axial stiffness term K_a. These relationships are experimentally verified in Section III-B.

III. Experiments and Results

A. Shape Sensing Calibration

Prior to inserting the FBG triplet into the COAST guidewire robot, the sensor is calibrated (Fig. 3). The FBG triplet is placed within a calibration plate, fabricated using 3D printing (Projet 5600, 3D Systems, South Carolina, USA), which consists of constant curvature grooves (Fig. 3(a)). This was used to compute the distances from each of the three fiber cores to the central axis of the FBG triplet for each sensing segment $\mathbf{d}_j = [d_{j,1}, d_{j,2}, d_{j,3}]$. The distances for each grating can be calibrated by optimizing a multi-objective function that minimizes the error of the expected and measured curvature and strain values. These functions can be displayed below as $F_1(\mathbf{d}_j)$ and $F_2(\mathbf{d}_j)$:

$$F_1(\mathbf{d}_j) = \left\| \frac{\hat{\kappa}(\mathbf{d}_j) - \kappa}{\kappa} \right\|_1 \quad F_2(\mathbf{d}_j) = \|\hat{\varepsilon}(\mathbf{d}_j) - \varepsilon\|_1 \tag{24}$$

where $\hat{\kappa}(d_j)$ and $\hat{\varepsilon}(d_j)$ are the estimated curvatures and strains for sensing segment j, respectively, κ is the groundtruth curvature of the calibration plate, and the expected axial strain of the FBG triplet, ε, is zero. Due to the scale difference between the curvature and strain errors, each of the above functions is normalized using the method presented in [30], resulting in the following optimization program:

$$\mathbf{d}_j = \underset{\mathbf{d}_j \in \mathbb{R}^3}{\operatorname{argmin}} \frac{F_1(\mathbf{d}_j) - F_1^{\circ}}{F_{1,max} - F_1^{\circ}} + \frac{F_2(\mathbf{d}_j) - F_2^{\circ}}{F_{2,\max} - F_2^{\circ}} \; j = 1, 2, 3 \tag{25}$$

$$\text{where } F_{1,max} = F_1(\arg\min_{\mathbf{d}_j \in \mathbb{R}^3} F_2(\mathbf{d}_j)) \text{ and } F_{2,max} = F_2(\arg\min_{\mathbf{d}_j \in \mathbb{R}^3} F_1(\mathbf{d}_j)) \tag{26}$$

where F_1° and F_2°, the ideal values of each function, are 0, indicating no error. These optimization programs are run for each sensing segment using the BFGS quasi-Newton algorithm in the MATLAB optimization toolbox.

B. Tip Force Validation

To fit the model proposed in Section II-D, the guidewire is first clamped at the base of the force sensing tip using a 3D-printed clamp to radially compress the guidewire in place. The tip is then probed several times with a 6 axis force sensor (ATI Nano17, ATI Industrial Automation, NC, USA) attached to a linear motion stage to record the forces being applied for a variety of loading directions by rotating the guidewire and adjusting the placement of the probe. The force data is filtered through a lowpass filter with a cutoff frequency of 5 Hz since the probing was conducted in a quasi-static state. Throughout probing, FBG readings are captured in addition to images from both the side and top planes. The calibration data is shown in Fig. 4(a-1) for the lateral forces along with the linear regression ($R^2 - \text{value} = 0.95$) for the force-curvature relationship where K_l is determined to be $6.54\ \text{N/mm}^{-1}$. Similarly, the calibration, along with the regression line ($R^2 - \text{value} = 0.81$), for the axial force-strain relationship is shown in Fig. 4(a-2) where the coefficient, K_a, is determined to be 1405.51 N. The time-series estimation for a primarily lateral force trial are shown in Fig. 4(b) where Fig. 4(b-1) shows the lateral force estimation while Figs. 4(b-2) and 4(b-3) show the estimated axial force, and overall force magnitude. For this test, the Root Mean Square Error (RMSE) for the lateral force, axial force, and force magnitude are determined to be 0.009 N, 0.015 N, and 0.010 N respectively. Similarly, the estimations for an axial loading with minor lateral forces are shown for the lateral (Fig. 4(c-1)), axial (Fig. 4(c-2)), and overall force magnitude (Fig. 4(c-3)) with an RMSE of 0.009 N, 0.031 N, and 0.029 N respectively. For probing experiments with the base of the tip fixed, consisting of two primarily axial and eight primarily lateral trials, the average RMSE was 0.008 N, 0.017 N, and 0.014 N for the lateral forces, axial forces, and overall force magnitudes respectively.

C. Simultaneous Shape and Force Sensing

To validate the FBG-based shape reconstruction and force estimation in the presence of external loading, the guidewire was operated in several motion profiles and made to contact the force sensor. Throughout this, images of the guidewire and force sensor measurements were collected to compare with the estimated values produced from the FBG readings.

To validate the real-time shape estimation, two CMOS cameras (CS165MU/M, Thorlabs, Newton, NJ) imaged the guidewire from perpendicular imaging planes with a conversion factor of 0.048 mm/pixel. Thresholding was used to extract the guidewire. Then a multivariate adaptive regression spline (MARS), implemented using the ARESLab toolbox, was used to find the centerline of the guidewire in each image [31], [32]. The shape of the guidewire

in 3D was then reconstructed using the centerline coordinates in the two orthogonal planes. The FBG-based shape reconstruction was aligned with the MARS centerline at the base of the sensing section which was considered to be 2.2 mm before the proximal end of the first sensing segment.

Tests were performed to evaluate the shape reconstruction and force sensing accuracy while bending, advancing, or extending the outer tube of the guidewire. The shape sensing results are summarized in Table III. In the first test, the inner tube was retracted to expose a bending length of 20 mm, and the guidewire was bent using tendon actuation such that the side of the guidewire tip collided with the force sensor, causing a lateral force (Figs. 5(a) and 5(b)). The error in the FBG-based shape reconstruction at the tip of the guidewire is shown in Fig. 5(c), and the FBG-based force estimation (Fig. 5(d)) had an RMSE of 0.005 N. The 3D shape reconstructions can be seen in Fig. 5(e).

In the second test, the guidewire was advanced to axially contact the force sensor with the three concentric tubes in the home configuration by translation of the guidewire stage which holds the actuation system (Figs. 6(a) and 6(b)). The error in the FBG-based shape reconstruction is shown in Fig. 6(c), and the force estimation (Fig. 6(d)) had an RMSE of 0.015 N. The 3D shape reconstructions can be seen in Fig. 6(e) where the different methods overlap.

Finally, the tendon was actuated to bend the guidewire with the inner tube retracted to expose a 20 mm bending length. The tendon actuation was then held constant as the outer tube was extended to axially contact the force sensor. The outer tube was then retracted, and the middle tube was straightened (Figs. 7(a) and 7(b)). The error in the FBG-based shape reconstruction is shown in Fig. 7(c), and the force estimation (Fig. 7(d)) had an RMSE of 0.027 N. The 3D shape reconstructions can be seen in Fig. 7(e) where the most distinction between reconstruction methods can be seen when the outer tube is partially extended.

IV. Discussion

This paper achieved FBG-based shape sensing of an unconstrained actuated COAST guidewire sample. The reconstruction methods showed similar accuracy for the middle tube bending and guidewire advancing motions. For each of these tests, the RMSE and maximum error values of the different reconstruction methods were within a range of approximately 0.05 mm and 0.11 mm, respectively. Larger differences in accuracy occurred during the middle tube bending and outer tube extension motion. Method 3 showed a higher error during portions of the outer tube extension with the bent middle tube resulting in an RMSE that was 0.49 mm greater than method 4. Method 1 showed the largest maximum error which was 0.37 mm greater than method 4. Reconstruction methods with similar accuracy for the desired motions can potentially be distinguished by other metrics such as computational efficiency for future implementation in real-time applications. One source of error in all shape reconstructions was the precurvature of the outer tube which caused the notched section of the outer tube to deflect where unsupported by the middle tube. In this paper, no grating was placed exactly at the junction between the bending segment and the force sensing tip, where this precurvature caused deflection when the outer tube was retracted. It is

hypothesized that the shape sensing accuracy will improve if a sensing segment is located at this junction.

FBG-based force sensing at the tip of the guidewire was achieved both when the force sensing tip was constrained and unconstrained. The accuracy of force sensing when actuating the guidewire was comparable to the constrained force sensing tip. The error was largest when the outer tube was extended into the force sensor. We hypothesize this to be caused by the flexibility of the notched section of the outer tube once it is extended past both the inner and middle tubes. Extending the outer tube into the force sensor was observed to cause it to bend and change shape, altering the direction of the force rather than remaining axial to the force sensor.

V. Conclusion

In this work, we enabled the COAST guidewire robot with shape and tip force sensing capabilities to provide feedback for control of the guidewire and to reduce the risk of vessel damage or perforation. Future works aim to improve shape sensing through the use of multi-core fibers and informed grating placement. Force sensing will be improved by developing models which incorporate the more proximal segments of the guidewire as well as the force sensing tip. Future work will also incorporate image feedback into the control loop for localizing the FBG-based reconstruction and improved teleoperated control for clinicians.

Acknowledgments

Research reported in this publication was supported in part by the National Heart, Lung, And Blood Institute of the National Institutes of Health under Award Number R01HL144714 and the National Science Foundation Graduate Research Fellowship under Grant No. DGE-2039655. The content, opinions, findings, and conclusions or recommendations expressed in this material are solely the responsibility of the authors and do not necessarily represent the official views of the National Institutes of Health or the National Science Foundation.

References

[1]. “Cardiovascular diseases (CVDs),” Who.int. [Online]. https://www.who.int/en/news-room/fact-sheets/detail/cardiovascular-diseases-(cvds), accessed: 2022-12-15.

[2]. Chitalia Y, Wang X, and Desai JP, “Design, modeling and control of a 2-DoF robotic guidewire,” in 2018 IEEE International Conference on Robotics and Automation (ICRA), 2018, pp. 32–37.

[3]. Tung AT, Park B-H, Niemeyer G, and Liang DH, “Laser-machined shape memory alloy actuators for active catheters,” IEEE/ASME Transactions on Mechatronics, vol. 12, no. 4, pp. 439–446, 2007.

[4]. Dupont PE, Lock J, Itkowitz B, and Butler E, “Design and control of concentric-tube robots,” IEEE Transactions on Robotics, vol. 26, no. 2 , pp. 209–225, 2009.

[5]. Webster RJ, Romano JM, and Cowan NJ, “Mechanics of precurved-tube continuum robots,” IEEE Transactions on Robotics, vol. 25, no. 1, pp. 67–78, 2009.

[6]. Kim J, Nguyen PB, Kang B, Choi E, Park J-O, and Kim C-S, “A novel tip-positioning control of a magnetically steerable guidewire in sharply curved blood vessel for percutaneous coronary intervention,” International Journal of Control, Automation and Systems, vol. 17, no. 8, pp. 2069–2082, 2019.

[7]. Shi C, Luo X, Qi P, Li T, Song S, Najdovski Z, Fukuda T, and Ren H, “Shape sensing techniques for continuum robots in minimally invasive surgery: A survey,” IEEE Transactions on Biomedical Engineering, vol. 64, no. 8, pp. 1665–1678, 2016. [PubMed: 27810796]

[8]. Henken KR, Dankelman J, van den Dobbelsteen JJ, Cheng LK, and van der Heiden MS, “Error analysis of FBG-based shape sensors for medical needle tracking,” IEEE/ASME Transactions on Mechatronics, vol. 19, no. 5, pp. 1523–1531, 2013.

[9]. Dong Z, Wang X, Fang G, He Z, Ho JD-L, Cheung C-L, Tang WL, Xie X, Liang L, Chang H-C et al. , “Shape tracking and feedback control of cardiac catheter using MRI-guided robotic platform—validation with pulmonary vein isolation simulator in MRI,” IEEE Transactions on Robotics, vol. 38, no. 5, pp. 2781–2798, 2022.

[10]. Denasi A, Khan F, Boskma KJ, Kaya M, Hennersperger C, Göbl R, Tirindelli M, Navab N, and Misra S, “An observer-based fusion method using multicore optical shape sensors and ultrasound images for magnetically-actuated catheters,” in 2018 IEEE International Conference on Robotics and Automation (ICRA). IEEE, 2018, pp. 50–57.

[11]. Stathopoulos I, Panagopoulos G, Kossidas K, Jimenez M, and Garratt K, “Guidewire-induced coronary artery perforation and tamponade during PCI: in-hospital outcomes and impact on long-term survival,” Journal of Invasive Cardiology, vol. 26, no. 8, 2014.

[12]. Brumfiel TA, Sarma A, and Desai JP, “Towards FBG-based end-effector force estimation for a steerable continuum robot,” in 2022 International Symposium on Medical Robotics (ISMR), 2022, pp. 1–7.

[13]. Khan F, Roesthuis RJ, and Misra S, “Force sensing in continuum manipulators using fiber Bragg grating sensors,” in 2017 IEEE/RSJ International Conference on Intelligent Robots and Systems (IROS), 2017, pp. 2531–2536.

[14]. Xu K and Simaan N, “An investigation of the intrinsic force sensing capabilities of continuum robots,” IEEE Transactions on Robotics, vol. 24 , no. 3, pp. 576–587, 2008.

[15]. Back J, Manwell T, Karim R, Rhode K, Althoefer K, and Liu H, “Catheter contact force estimation from shape detection using a real-time Cosserat rod model,” in 2015 IEEE/RSJ International Conference on Intelligent Robots and Systems (IROS), 2015, pp. 2037–2042.

[16]. Xiao Q and Chen Y, “Efficient force estimation for continuum robot,” arXiv preprint arXiv:2109.12469, 2021.

[17]. Qiao Q, Willems D, Borghesan G, Ourak M, De Schutter J, and Vander Poorten E, “Estimating and localizing external forces applied on flexible instruments by shape sensing,” in 2019 19th International Conference on Advanced Robotics (ICAR). IEEE, 2019, pp. 227–233.

[18]. Feng F, Hong W, and Xie L, “A learning-based tip contact force estimation method for tendon-driven continuum manipulator,” Scientific Reports, vol. 11, no. 1, pp. 1–11, 2021. [PubMed: 33414495]

[19]. Ha XT, Wu D, Lai C-F, Ourak M, Borghesan G, Menciassi A, and Poorten EV, “Contact localization of continuum and flexible robot using data-driven approach,” IEEE Robotics and Automation Letters, vol. 7, no. 3, pp. 6910–6917, 2022.

[20]. Donat H, Lilge S, Burgner-Kahrs J, and Steil JJ, “Estimating tip contact forces for concentric tube continuum robots based on backbone deflection,” IEEE Transactions on Medical Robotics and Bionics, vol. 2, no. 4, pp. 619–630, 2020.

[21]. Jeong S, Chitalia Y, and Desai JP, “Design, modeling, and control of a coaxially aligned steerable (COAST) guidewire robot,” IEEE Robotics and Automation Letters, vol. 5, no. 3, pp. 4947–4954, 2020.

[22]. Sarma A, Brumfiel TA, Chitalia Y, and Desai JP, “Kinematic modeling and Jacobian-based control of the COAST guidewire robot,” IEEE Transactions on Medical Robotics and Bionics, vol. 4, no. 4, pp. 967–975, 2022. [PubMed: 37790986]

[23]. Ravigopal SR, Brumfiel TA, and Desai JP, “Automated motion control of the COAST robotic guidewire under fluoroscopic guidance,” in 2021 International Symposium on Medical Robotics (ISMR), 2021, pp. 1–7.

[24]. Deaton NJ, Sheft M, and Desai JP, “Towards FBG-based shape sensing and sensor drift for a steerable needle,” IEEE/ASME Transactions on Mechatronics, pp. 1–12, 2023, doi: 10.1109/TMECH.2023.3239750.

[25]. Grattan K and Meggitt B, “Optical fiber sensor technology, vol. 2—devices and technology,” Chapmann & Hall, 1998.

[26]. Lee B, “Review of the present status of optical fiber sensors,” Optical Fiber Technology, vol. 9, no. 2, pp. 57–79, 2003.

[27]. Roesthuis RJ, Kemp M, van den Dobbelsteen JJ, and Misra S, “Three-dimensional needle shape reconstruction using an array of fiber Bragg grating sensors,” IEEE/ASME Transactions on Mechatronics, vol. 19, no. 4, pp. 1115–1126, 2014.

[28]. Moore JP and Rogge MD, “Shape sensing using multi-core fiber optic cable and parametric curve solutions,” Optics Express, vol. 20, no. 3, pp. 2967–2973, 2012. [PubMed: 22330534]

[29]. Sefati S, Hegeman R, Alambeigi F, Iordachita I, Kazanzides P, Khanuja H, Taylor RH, and Armand M, “A surgical robotic system for treatment of pelvic osteolysis using an FBG-equipped continuum manipulator and flexible instruments,” IEEE/ASME Transactions on Mechatronics, vol. 26, no. 1, pp. 369–380, 2020. [PubMed: 34025108]

[30]. Marler RT and Arora JS, “Survey of multi-objective optimization methods for engineering,” Structural and Multidisciplinary Optimization, vol. 26, no. 6, pp. 369–395, 2004.

[31]. Friedman JH, “Multivariate adaptive regression splines,” The Annals of Statistics, pp. 1–67, 1991.

[32]. Jekabsons G, “ARESLab: Adaptive regression splines toolbox for MATLAB/Octave,” 2016, available at http://www.cs.rtu.lv/jekabsons/.

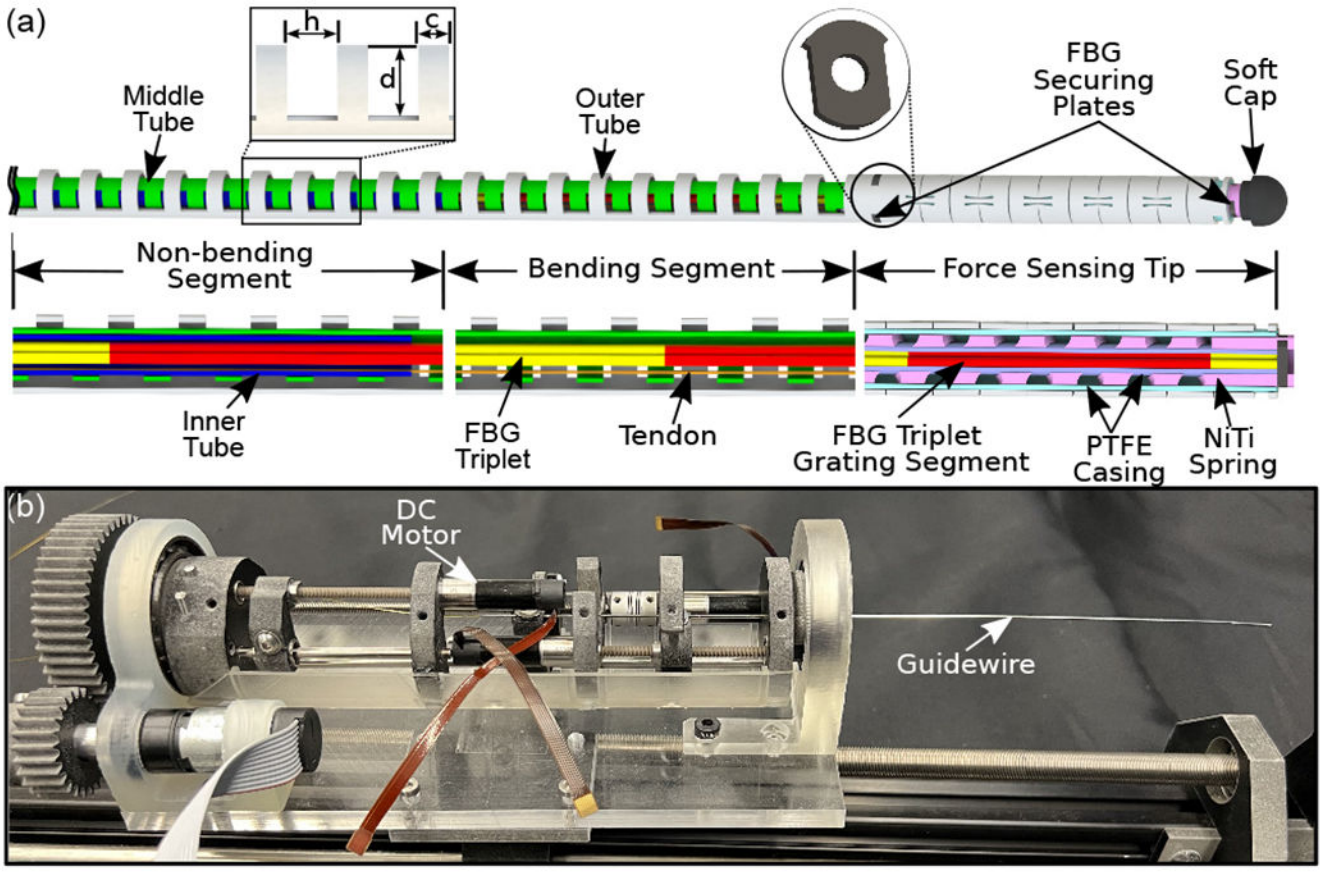

Fig. 1:

Schematic of (a) the COAST guidewire robot with integrated shape and force sensing with cross sections indicating the non-bending, bending, and force sensing segments, (left inset) a diagram of the notch parameters, and (right inset) an FBG securing plate. (b) The COAST guidewire assembled in the compact actuation system.

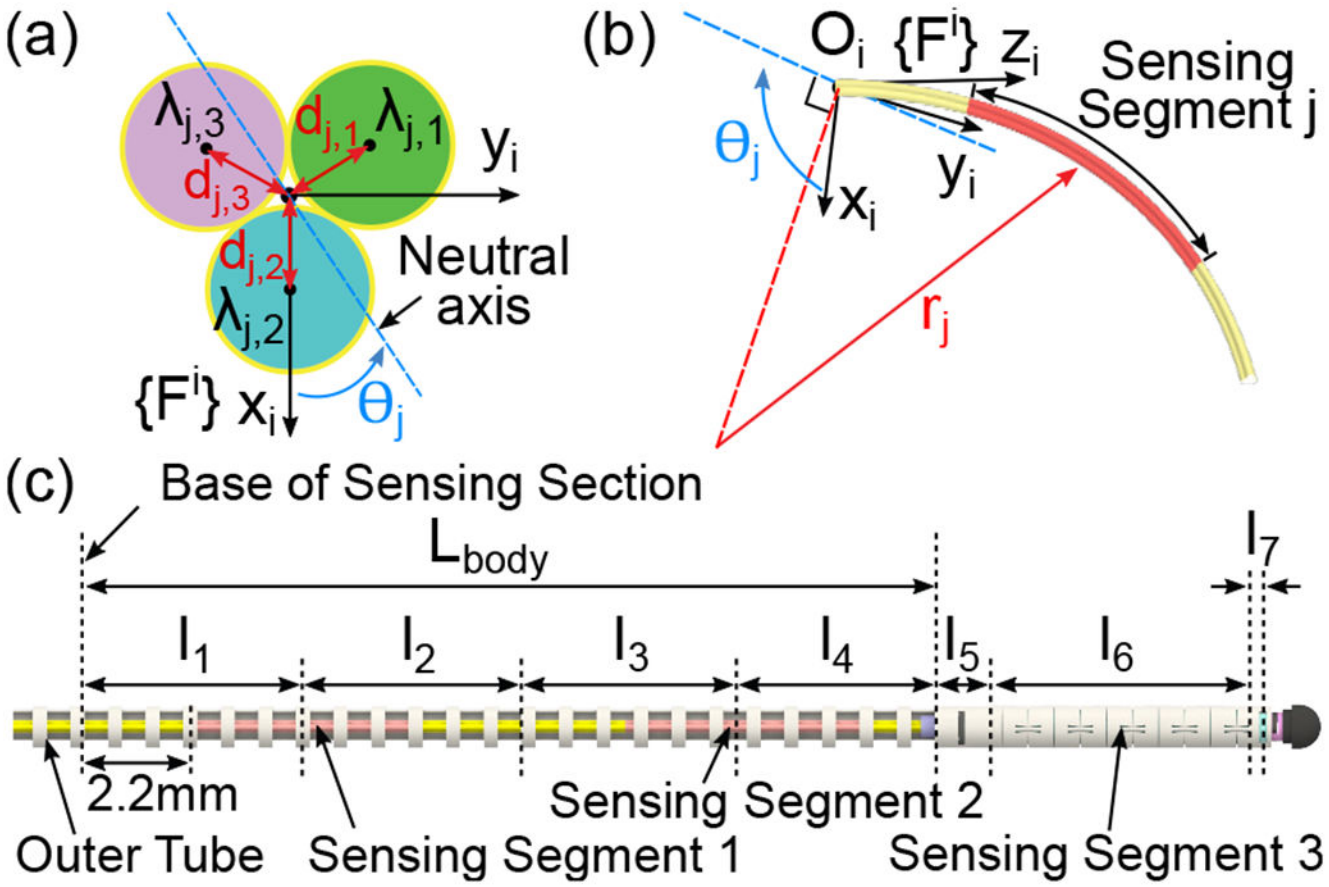

Fig. 2:
Shape sensing model: (a) cross-section of the sensor, (b) 3D view of the sensor, (c) outer tube and FBG triplet.

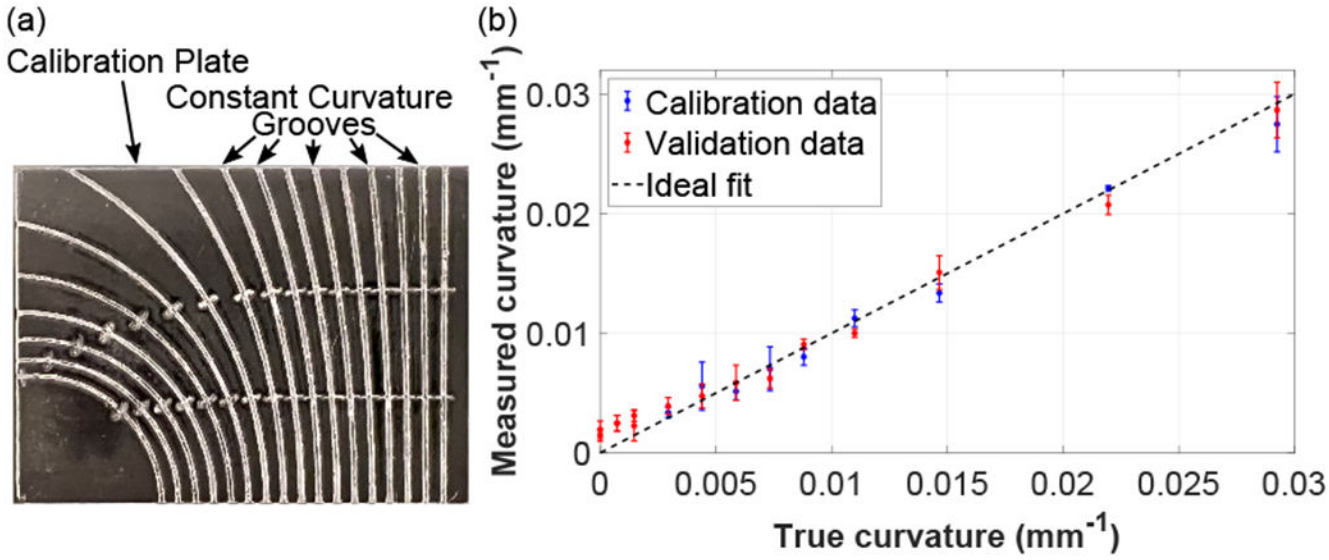

Fig. 3:
FBG sensor calibration: (a) calibration plate and (b) calibration results. Using the validation data set, $R^2 = 0.96$.

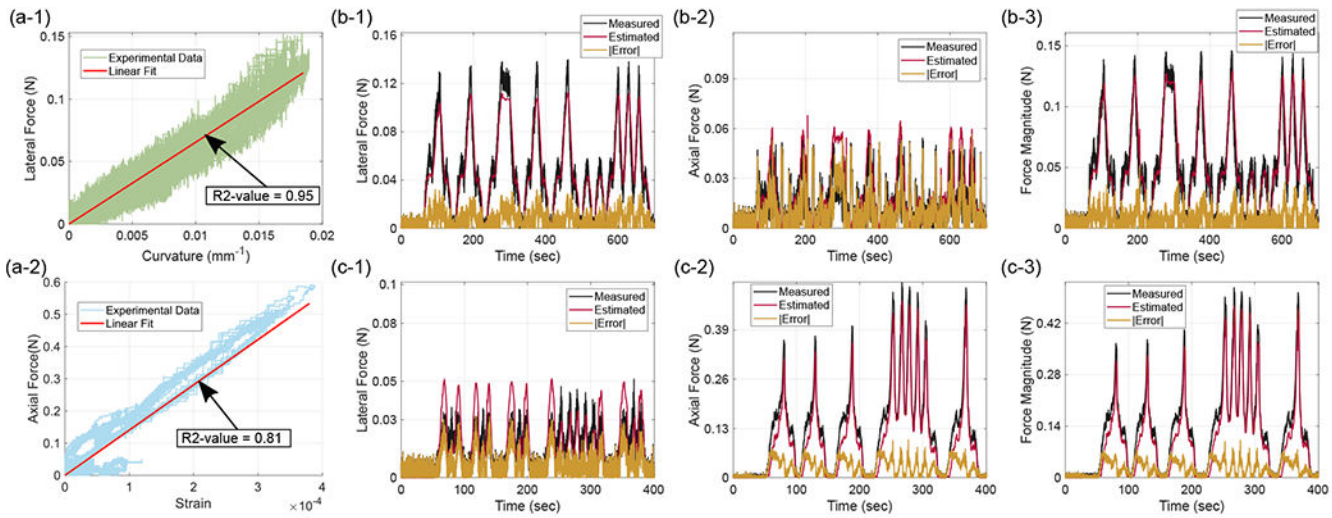

Fig. 4:

Force sensing tip calibration for (a-1) lateral forces and (a-2) axial forces. Validation through probing with primarily lateral forces showing (b-1) lateral forces, (b-2) axial forces, and (b-3) force magnitudes of the measured values, FBG-based estimates, and the absolute error as well as for primarily axial tests showing (c-1) lateral forces, (c-2) axial forces, and (c-3) force magnitudes.

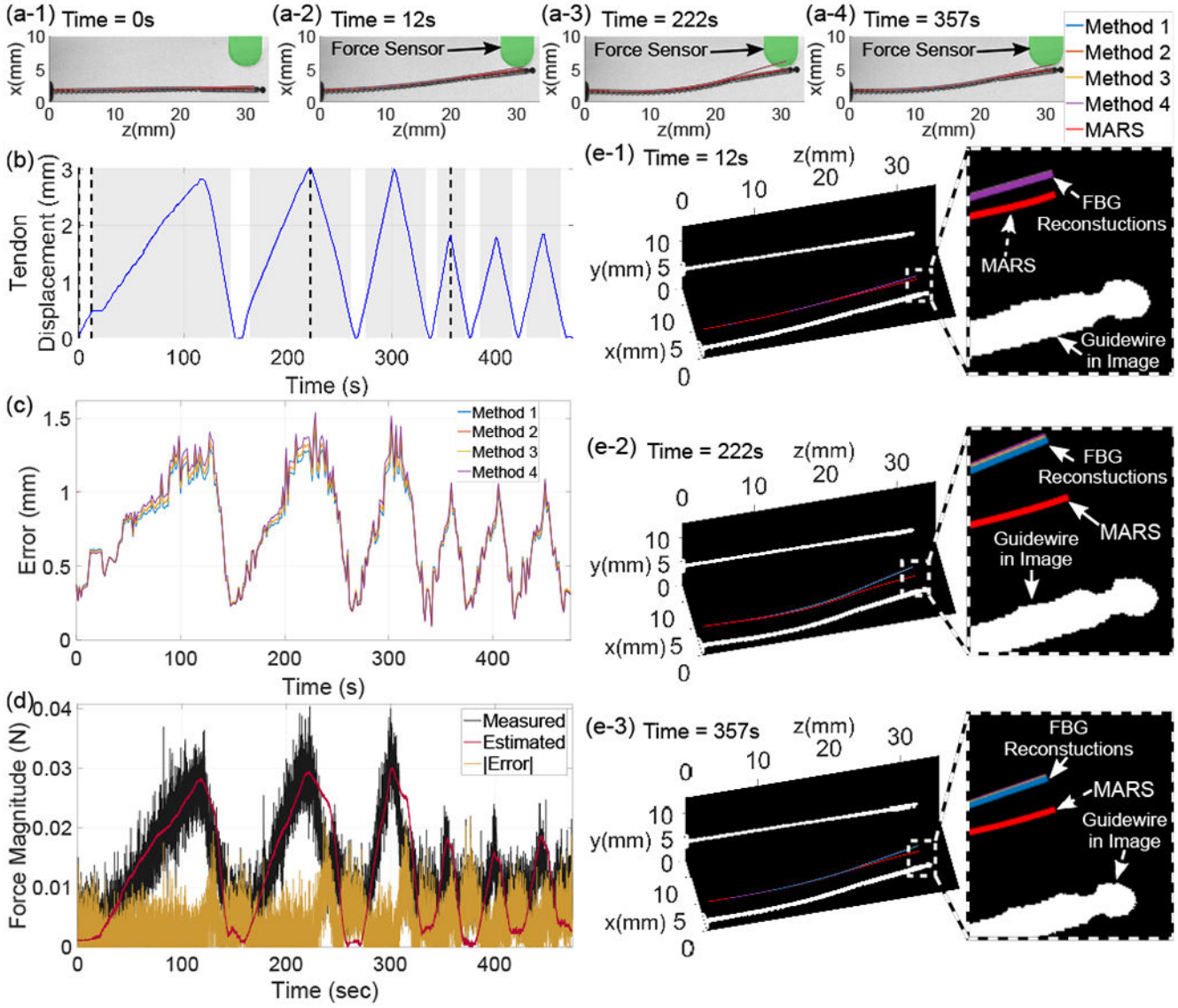

Fig. 5:

Tendon-actuated bending of the guidewire to laterally contact the force sensor: (a) xz-plane images with the MARS centerline and FBG-based shape reconstructions at different timestamps which are marked by vertical dashed lines in (b) the tendon displacement, (c) 3D position error of the FBG-based reconstructions at the tip of the guidewire, (d) the force magnitude of the measured values, FBG-based estimates, and absolute error, and (e) 3D reconstructions of the guidewire.

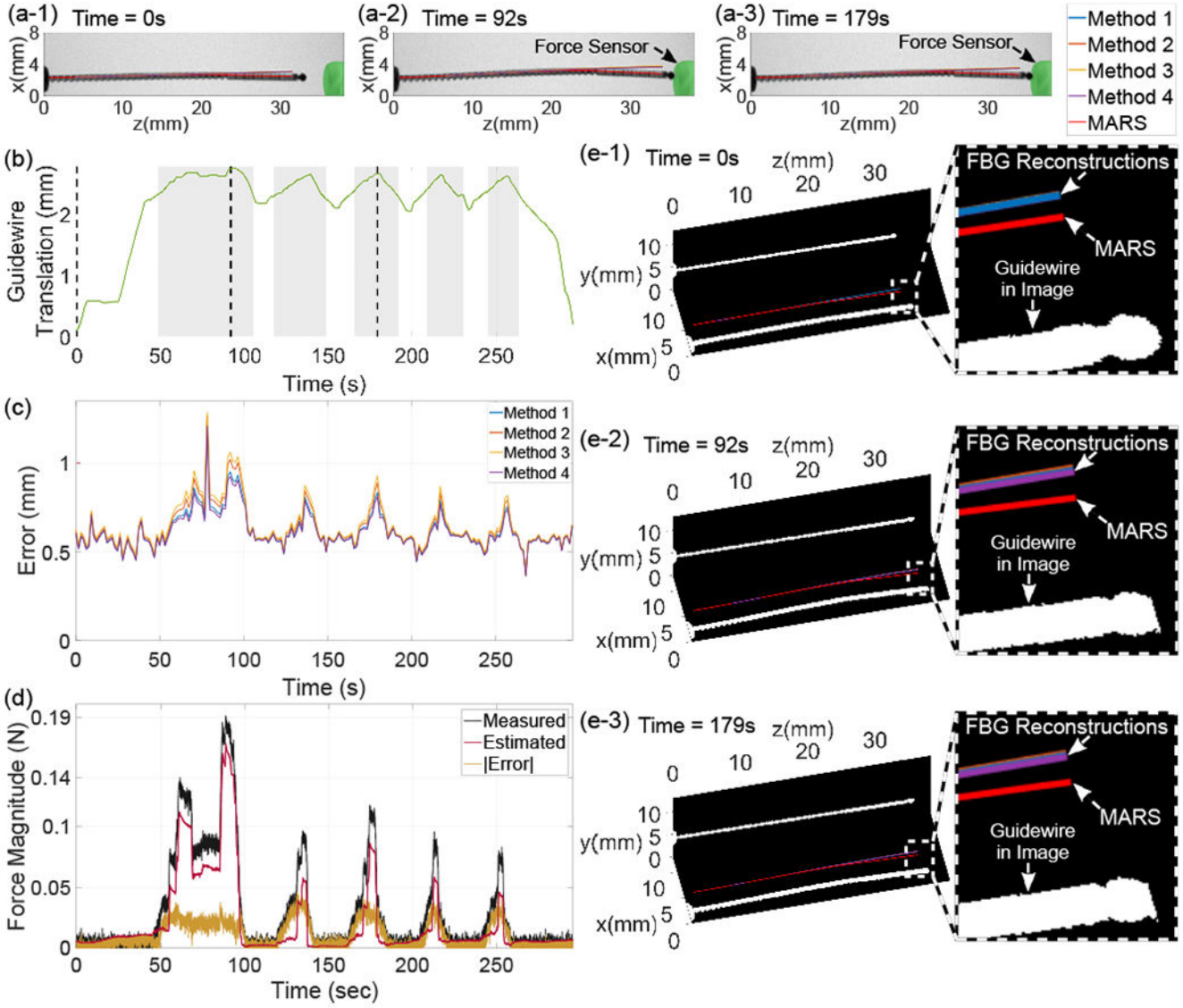

Fig. 6:

Translation of the guidewire to axially contact the force sensor: (a) xz-plane images with the MARS centerline and FBG-based shape reconstructions at different timestamps which are marked by vertical dashed lines in (b) the guidewire stage translation, (c) 3D position error of the FBG-based reconstructions at the tip of the guidewire, (d) the force magnitude of the measured values, FBG-based estimates, and absolute error, and (e) 3D reconstructions of the guidewire.

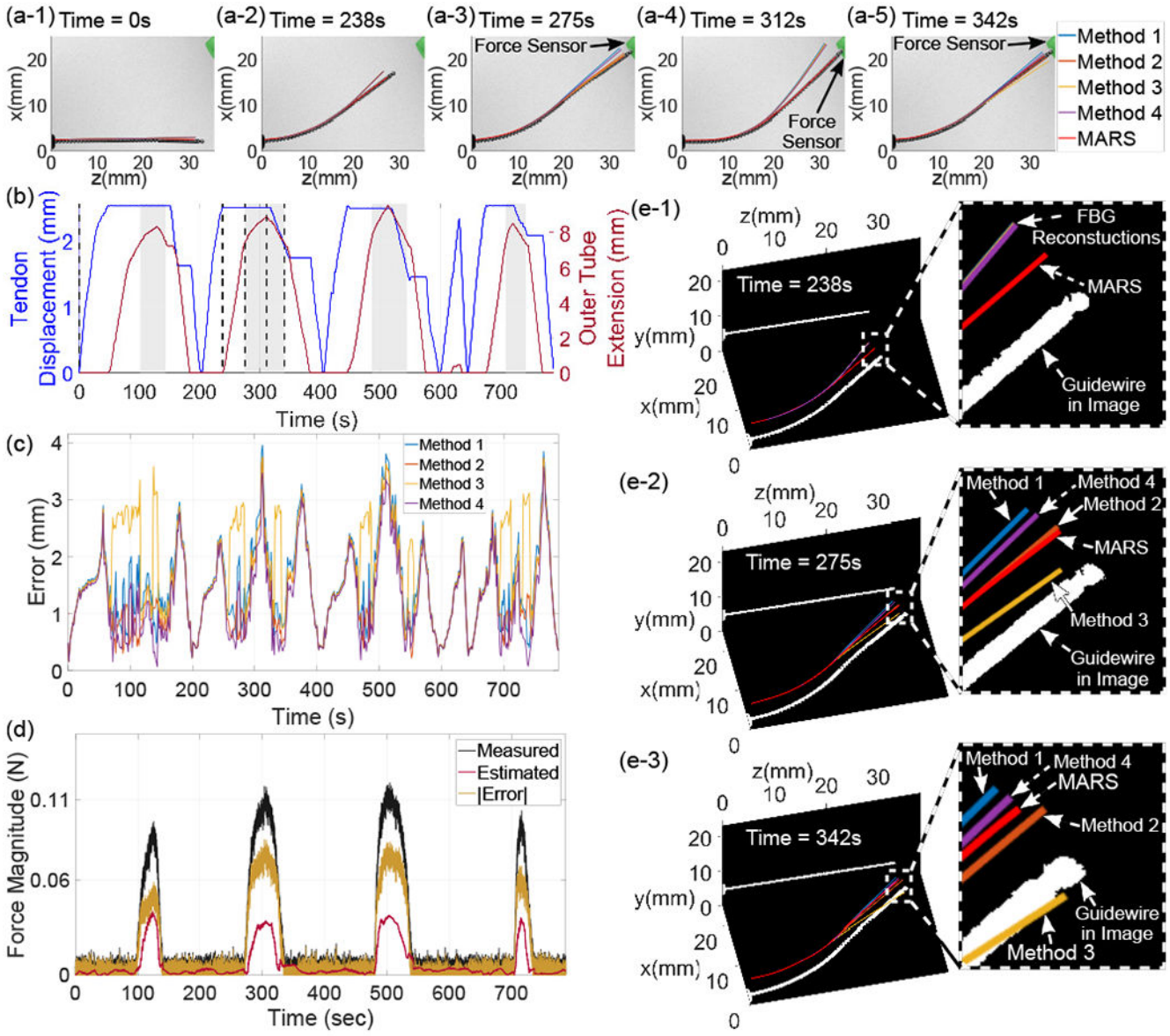

Fig. 7:

Tendon-actuated bending and outer tube extension of the guidewire to axially contact the force sensor: (a) xz-plane images with the MARS centerline and FBG-based shape reconstructions at different timestamps which are marked by vertical dashed lines in (b) the tendon displacement and outer tube extension of the guidewire, (c) 3D position error of the FBG-based reconstructions at the tip of the guidewire, (d) the force magnitude of the measured values, FBG-based estimates, and absolute error, and (e) 3D reconstructions of the guidewire.

TABLE I:

Specifications of the COAST guidewire.

Items	Outer tube	Middle tube	Inner tube	Tendon
Total length (mm)	154	170	200	296
Notched length (mm)	112.8	48.5	-	-
Outer diameter (mm)	0.89	0.60	0.48	0.076
Inner diameter (mm)	0.77	0.52	0.40	-
Notch depth, d (mm)	0.75	0.39	-	-
Notch width, h (mm)	0.51	0.50	-	-
Notch spacing, c (mm)	0.29	0.30	-	-

TABLE II:

Reconstruction lengths.

l_1 (mm)	l_2 (mm)	l_3 (mm)	l_4 (mm)	l_5 (mm)	l_6 (mm)	l_7 (mm)	L_{body}
4.695	4.695	4.695	5.156	1.983	5.626	0.75	$l_1+l_2+l_3+l_4$

TABLE III:

Results for shape reconstruction.

Reconstruction	Bend Middle Tube		Advance Guidewire		Bend Middle and Extend Outer Tubes	
	RMSE (mm)	Max Error (mm)	RMSE (mm)	Max Error (mm)	RMSE (mm)	Max Error (mm)
Method 1	0.80	1.43	0.63	1.23	1.69	3.96
Method 2	0.82	1.48	0.65	1.27	1.57	3.74
Method 3	0.82	1.48	0.66	1.28	1.94	3.76
Method 4	0.85	1.54	0.62	1.21	1.45	3.59